

# Stereological characterization of the major cell lineages in the mouse dorsal dentate gyrus

**Joshua D. Rieskamp<sup>1,2</sup>, Patricia Sarchet<sup>2</sup>, Bryon M. Smith<sup>2</sup>, Elizabeth D. Kirby<sup>2,3,4\*</sup>,**

<sup>1</sup>Neuroscience Graduate Program, The Ohio State University, Columbus, OH, United States.

<sup>2</sup>Department of Psychology, The Ohio State University, Columbus, OH, United States.

<sup>3</sup>Department of Neuroscience, The Ohio State University, Columbus, OH, United States.

<sup>4</sup>Center for Chronic Brain Injury, The Ohio State University, Columbus, OH, United States.

## **\* Correspondence:**

Elizabeth Kirby

Kirby.224@osu.edu

**Keywords:** stereology, hippocampus, dentate gyrus, neurons, glia, neurogenesis

## **Abstract**

The dentate gyrus (DG) subregion of the mammalian hippocampus mediates critical cognitive processes related to memory and is a site of continuous adult neurogenesis. The mechanisms by which diverse neuronal and non-neuronal cell populations regulate adult neurogenesis and contribute to DG function are an intense, current focus of research. Obtaining an accurate estimate of DG cellular composition is vital for understanding how distinct cell populations contribute to hippocampal function. However, most studies examine only a select few cell types, and the reported numbers vary considerably. Here, we apply consistent stereological methods within a single study to estimate cell density for the major lineages in the dorsal DG of adult mice. Using immunohistochemical phenotypic markers, we quantified cell density for radial glia-like cells, neuronal intermediate progenitors, neuroblasts/immature neurons, mature neurons, stellate astrocytes, oligodendrocytes and their progenitors, microglia, and vascular endothelial cells. The value of a unified dataset was evident when evaluating the relative abundance of different cell types. Ratios of neurons:astrocytes generated using counts of each cell type obtained from separate studies could range from approximately 4.6:1 to 113:1. In contrast, our reported estimate of roughly 12 neurons:1 astrocyte is consistent with the 9:1 ratio from previous work where both cell types were quantified within the same study. This highlights the utility of counts obtained within a single study to make accurate comparisons of relative cell type abundance. We expect the data reported here will facilitate efforts to refine hypotheses about the functional contributions of DG cell populations.

## **Introduction**

The mammalian hippocampus is well studied for its role in episodic memory, spatial navigation, and mood regulation (Strange et al., 2014). Within the hippocampal circuit, the dentate gyrus (DG) subregion mediates crucial computational processes related to memory, including pattern separation (Knierim and Neunuebel, 2016; Yassa and Stark, 2011). These proposed functional roles likely relate to the distinct neuroanatomical features of the DG, including its organization along the longitudinal (dorsal-ventral or septal-temporal) axis (Strange et al., 2014).

One prominent feature of the DG that sets it apart from most adult brain circuits is the continuous generation and circuit integration of granule neurons throughout the lifespan. Adult hippocampal neurogenesis is known to occur in most mammals, possibly including humans (Gonçalves et al., 2016; Moreno-Jiménez et al., 2019; but see Sorrells et al., 2018). However, precisely how adult neurogenesis relates to the function of the DG is still an area of intense investigation (Miller and Sahay, 2019). Another topic of great interest is identifying the factors that permit functional integration of immature neurons in the adult nervous system, as this knowledge will be instrumental for designing rational strategies for regenerative therapies. Toward this end, recent studies have revealed that the maturation and integration of adult-born neurons is heavily influenced by neighboring cell populations including developmentally born mature neurons, local astroglia, and even undifferentiated neural precursor cells (Kirschen et al., 2017; Sultan et al., 2015; Tang et al., 2019).

To evaluate the functional contributions of distinct DG cell populations, it is useful to know their relative population sizes. For example, computational models seeking to explain the function of adult neurogenesis are calibrated by estimates of the relative numbers of developmentally born granule neurons versus adult-born neurons (Aimone et al., 2009). Given the active role of various non-neuronal cell types in hippocampal physiology, accurate estimates of glial and endothelial populations could similarly calibrate computational models and theoretical frameworks of dentate gyrus function.

Most stereological studies of the DG examine a select few cell types, and while efforts have been made to generate comprehensive atlases (Erö et al., 2018), these databases currently lack information about essential cell types within the DG such as neural precursor cells and their progeny. Therefore, one must combine multiple sources to obtain an estimate of DG cellular composition. However, numbers vary substantially across studies, even for commonly quantified cell types such as granule neurons (Keller et al., 2018), leading to considerably different conclusions depending on which data is used to draw comparisons.

To circumvent this issue, here we apply consistent stereological methods within the same study to estimate the relative population size of the major lineages known to reside within the dorsal DG including neural, astroglial, oligodendroglial, microglial, and endothelial cells.

## Materials and Methods

**Animals.** All animal use was in accordance with institutional guidelines approved by the Ohio State University Institutional Animal Care and Use Committee and with recommendations of the National Institutes of Health Guide for the Care and Use of Laboratory Animals. C57BL/6 mice (5 male, 4 female) were acquired from Jackson Laboratories at 7 weeks of age and housed in a vivarium at Ohio State University with 24h ad libitum water and standard mouse chow on a 12h light-dark cycle for 1 week. Mice received one injection of 150 mg/kg bromodeoxyuridine (Sigma) dissolved in physiological saline, and 2h later were anesthetized with 87.5 mg/kg ketamine/12.5 mg/kg xylazine and transcardially perfused with 0.1 M phosphate buffered saline (PBS).

**Tissue processing.** Brains were fixed for 24h in 4% paraformaldehyde in 0.1 M phosphate buffer then equilibrated for at least 2 days in 30% sucrose in PBS, both at +4°C. They were then sliced on a freezing microtome (Leica) in a 1 in 12 series of 40 µm slices. Slices were stored in cryoprotectant at -20°C. Immunohistochemical staining was performed on free-floating sections as previously described (Smith et al., 2018). Briefly, sections were rinsed three times in PBS, incubated in blocking solution (1% normal donkey serum, 0.3% triton-X 100 in PBS) for 30 min then incubated in primary antibody diluted in blocking buffer overnight at 4°C on rotation. The next day, sections were rinsed and incubated in

secondary antibody in blocking solution at room temperature for 2 hours, followed by 10 min in Hoechst 33342 (Invitrogen) diluted 1:2000 in PBS. After rinsing, sections were mounted on superfrost plus glass slides (Fisher) and cover-slipped with Prolong Gold Anti-fade medium (Invitrogen). After drying, slides were stored in the dark at 4°C until imaging. For BrdU immunohistochemical labeling, the above procedures were followed with the addition of a 30 min incubation in 2N HCl at 37°C to denature DNA before the blocking step.

**Stereological cell counts.** Stereological cell counts were performed in a single series of every 12th slice for each cell phenotype marker. Images of the dorsal DG were captured using Zeiss AxioImager.M2 microscope and a Zeiss MRc digital camera. Cells were counted at high magnification (100x with oil immersion for NeuN, 40x with oil immersion for all other markers) using the optical fractionator method (StereoInvestigator). The counting frame had an area of  $625 \mu\text{m}^2$  (NeuN) or  $10,000 \mu\text{m}^2$  (all other markers) and a height of 15  $\mu\text{m}$  with 5  $\mu\text{m}$  guard zones. Neurons, oligodendrocytes, and proliferating cells were all identified using the nuclear markers in **Table 1**. Endothelial cells, microglia, and neuroblasts/immature neurons were identified by the cytoplasmic markers in **Table 1** surrounding a Hoechst+ nucleus. Radial glia-like neural precursor cells (RGLs) were identified as SOX2+ nuclei in the subgranular zone surrounded by GFAP+ cytoplasm with an apical process extending into the granular cell layer. Neural intermediate progenitor cells (IPs) were identified as SOX2+ nuclei in the subgranular zone lacking cytoplasmic GFAP. Astrocytes were identified as SOX2+ cells with GFAP+ stellate processes located in any DG subregion. The mean number of cells counted for each marker are listed in **Table 2**.

**Data analysis and statistics.** Cell density was calculated from cell count divided by sampled DG tissue volume. Because immunohistochemical processing causes tissue shrinkage, sampled tissue volume was estimated using sampled area adjusted by the proportional change in measured post-processing tissue thickness (i.e. thickness measured in 3 locations per slice using StereoInvestigator versus the sliced thickness of 40  $\mu\text{m}$ ). Mean thickness measurements obtained for each round of immunostaining are reported in **Figure 2**. For each cell type, cell densities in males and females were compared using an unpaired, two-tailed t-test (Prism GraphPad).

**Cell distribution.** Incomplete antibody penetration can interfere with obtaining accurate stereological estimates. We verified complete antibody penetration by comparing the number of cells for each marker counted in 5 consecutive 1  $\mu\text{m}$  z-sections in the middle of the tissue compared to the 5 consecutive 1  $\mu\text{m}$  z-sections immediately below the guard zone (top). We observed similar counts obtained from the middle z-sections compared to the top, suggesting uniform antibody penetration (**Table 2**).

**Error estimates.** Previous work suggests that the Gundersen-Jensen coefficient of error (CE) estimator (Gundersen et al., 1999) is useful for evaluating the precision of stereological estimates in the hippocampal structure (Slomianka and West, 2005). The mean Gundersen-Jensen CE for each cell type is reported in **Table 2**.

## Results

We used immunohistochemistry to identify cells expressing phenotypic markers of the major lineages known to reside within the dentate gyrus (DG): ectodermal (neural, astroglial, oligodendroglial) and mesodermal (microglia, vascular endothelial). Cells density estimates were derived for adult wildtype C57BL/6 mice using the optical fractionator method to count cells within a region of interest (ROI) encompassing all layers of the DG at the dorsal (septal/rostral) pole of the dorsal-ventral axis (**Figure 1A-B**).

## Ectodermal lineage cells

### *Neural precursor cells and astroglia*

Unique to the DG subregion of the hippocampus is a population of neural precursor cells and their progeny. Because many of the protein markers expressed by adult neural precursors are also present in mature astrocytes (Semerci and Maletic-Savatic, 2016), we distinguished these cell populations based on a combination of SOX2 and GFAP immunolabeling along with cell morphology (Suh et al., 2007; **Figure 1C-E**). We identified radial glial-like neural precursors (RGLs) as having SOX2+ nuclei located in the subgranular zone (SGZ) and GFAP+ cytoplasm with a radial process extending into the granule cell layer (**Figure 1D-E**). The progeny of RGLs, neural intermediate progenitor cells (IPs), were identified as SOX2+ nuclei located in the SGZ that lacked GFAP+ cytoplasm (**Figure 1D-E**). Mature protoplasmic astrocytes had SOX2+ nuclei located in any region of the DG and GFAP+ cytoplasm with stellate processes (**Figure 1D-E**). We found that mature astrocytes were the most abundant of these three populations ( $8274.7 \pm 1109.7$ ,  $9232.4 \pm 1095.1$  cells/mm<sup>3</sup>, females and males, respectively) followed by IPs ( $4532.2 \pm 469.7$ ,  $5220.1 \pm 820.2$  cells/mm<sup>3</sup>), then RGLs ( $1364.9 \pm 132.0$ ,  $1228.6 \pm 59.5$  cells/mm<sup>3</sup>, **Figure 2A**). Males and females did not significantly differ in number of astrocytes ( $p>0.05$ ,  $t=0.61$ ), RGLs ( $p>0.05$ ,  $t=1.02$ ), or IPs ( $p>0.05$ ,  $t=0.68$ ).

### *Mitotically active cells*

To expand the quantification of progenitor cells, we used two markers of cellular mitosis. The adult DG contains various populations of mitotically active cells, which can be identified using endogenous cell cycle markers such as MCM2 or the exogenous S phase marker bromodeoxyuridine (BrdU) (von Bohlen und Halbach, 2011; Kuhn et al., 2016). Previous studies have shown that the majority of MCM2+ or recently BrdU-labeled cells in the DG are neural IPs located within the SGZ, with a sparser number of proliferative glial cells located outside the SGZ (Bonaguidi et al., 2011; Mandyam et al., 2007). Consistent with these previous findings, we found MCM2+ cells throughout the entire DG, but the greatest density was found within the SGZ (**Figure 1F-H**). To obtain counts most directly related to IP number, only MCM2+ cells in the SGZ were quantified. The density of MCM2+ IPs cells in the DG did not significantly differ between females and males ( $4324.1 \pm 1106.9$  vs  $3740.7 \pm 356.8$  cells/mm<sup>3</sup>,  $p>0.05$ ,  $t=0.55$ ) (**Figure 2A**). We obtained similar results quantifying BrdU+ cells after a single BrdU injection 2 hours before perfusion. BrdU labeled cells were found throughout the entire extent of the DG, but most commonly within the SGZ (**Figure 1I-K**). To obtain counts most directly related to number of IPs in S-phase, only BrdU+ cells in the SGZ were quantified. The density of BrdU-labeled IPs in the DG was not different between females and males ( $658.4 \pm 61.9$  vs  $597.3 \pm 162.1$  cells/mm<sup>3</sup>,  $p>0.05$ ,  $t=0.32$ ) and represented a smaller subset of cells than all cycling (i.e. MCM2+) cells, as expected (**Figure 2A**).

### *Neuronal cells*

Due to continuous neurogenesis throughout life, the rodent DG contains a mixture of granule neurons born at different stages of development. In the DG, doublecortin (DCX) marks neuroblasts and recently born, immature granule neurons, while NeuN+ marks the nuclei of various mature neuronal subtypes, the most abundant of which is mature granule neurons (Kuhn et al., 2016). As expected, DCX+ cells were located within the SGZ and inner third of the GCL (**Figure 1L-N**), and NeuN+ cells were densely packed in the GCL and more sparsely distributed throughout the hilus (**Figure 1 O-Q**). The density of DCX+ cells was similar in scale to MCM2+ and SOX2+ IPs and did not significantly differ between males and females ( $4820.5 \pm 656.4$  vs  $4924.7 \pm 376.0$  cells/mm<sup>3</sup>,  $p>0.05$ ,  $t=0.15$ , **Figure 2A**). NeuN+

cells were over 20-fold more numerous than DCX cells, and did not differ between females and males ( $100564.5 \pm 10848.3$  vs  $115109.3 \pm 13077.4$  cells/mm<sup>3</sup>,  $p>0.05$ ,  $t=0.83$ , **Figure 2A**).

### *Oligodendroglia*

We identified cells of the oligodendroglia lineage including oligodendrocyte progenitor cells (OPCs), newly formed oligodendrocytes, and mature myelinating oligodendrocytes based on Olig2 immunolabeling (Valério-Gomes et al., 2018). Olig2+ cells were mainly distributed throughout the molecular layer and hilus of the DG (**Figure 1R-T**). The density of oligodendroglia lineage cells was comparable to that of IPs and not different between females and males ( $4125.9 \pm 1213.0$  vs  $2610.7 \pm 333.1$  cells/mm<sup>3</sup>,  $p>0.05$ ,  $t=1.34$ , **Figure 2A**).

### **Mesodermal lineage cells**

#### *Microglia*

Iba1+ microglia were distributed throughout every region of the DG (**Figure 1U-W**) and were intermediate in density between oligodendroglial lineage cells and RGLs. No sex difference was found in Iba1+ cell density ( $2677.1 \pm 892.1$  vs  $1816.8 \pm 210.2$  cells/mm<sup>3</sup>,  $p>0.05$ ,  $t=1.05$ , **Figure 2A**).

#### *Vascular endothelial cells*

Vascular endothelial cells within the DG were identified by CD31 immunolabeling and formed vascular networks throughout all regions of the DG (**Figure 1X-Z**). The density of CD31+ cells was intermediate between the density of astrocytes and IPs, with no sex difference ( $6768.7 \pm 1067.3$  vs  $5849.0 \pm 639.4$  cells/mm<sup>3</sup>,  $p>0.05$ ,  $t=0.78$ , **Figure 2A**).

## **Cellular composition of the DG**

Cell density estimates for each cell marker quantified in the current study are depicted in **Figure 2A**. To facilitate comparisons with counts performed in sections cut to a commonly used thickness for free-floating immunohistochemistry, data is also presented as estimates of cell number in a 40  $\mu$ m slice (**Figure 2B**). In addition, we provide an estimate of relative population sizes for the major cell types quantified using mutually exclusive markers for RGLs, IPs, astrocytes, microglia, oligodendrocytes and endothelial cells (**Figure 2C**). This presentation of the data allows an appreciation of the approximate relative population sizes of the major cellular constituents of the DG.

## **Discussion**

We used stereologically-derived counts of neural, glial, and endothelial cell phenotypic markers to estimate the relative population densities of the major cell types within the dorsal DG. As expected, we found that the largest cell population was mature NeuN+ neurons, which outnumbered DCX+ neuroblasts and immature neurons by greater than 20-fold. GFAP+/SOX2+ stellate astrocytes were the second largest cell population in our study, followed closely by CD31+ vascular endothelial cells. The least abundant cell populations included GFAP-/SOX2+ neural intermediate progenitor cells (IPs), Olig2+ oligodendroglial lineage cells, Iba1+ microglia, and GFAP+/SOX2+ radial glia-like neural precursor cells (RGLs). Notably, we compared densities obtained from both male and female mice for each cell type and found no significant sex differences. While a previous study reports sex differences in DG astrocyte and microglia density (Mouton et al., 2002), the counts for males and females were obtained from separate rounds of tissue processing and counting. Though the authors made efforts to

maintain consistent methodology, small but systematic differences between cohorts could influence the results. In our study, where both sexes were processed and counted in a single cohort, we did not observe sex differences in astroglia, microglia, or any other cell type surveyed. To our knowledge, this is the first study to quantify all of these cell types in the DG of both sexes by applying the same methodology to a single cohort of mice.

Previous studies have estimated population size for each of the DG populations studied here individually. However, comparison of our data with previous work is complicated by the variability in population estimates across studies (Keller et al., 2018). For example, astrocyte density in the DG has been reported to be 5,533 cells/mm<sup>3</sup> (Olabarria et al., 2011), as well as 36,000 cells/mm<sup>3</sup> (Rajkowska et al., 2016). Estimates of mature neuronal density in the DG can range from 166,568 cells/mm<sup>3</sup> (Erö et al., 2018) to 625,080 cells/mm<sup>3</sup> (Kurt et al., 2004). This variability in cell type density estimates between studies could be attributed to methodological differences, such as use of different markers and anatomical boundaries, as well as differing computational methods for extrapolating from sampled counts to total population density estimates. Even within studies using unbiased stereology, small differences in sampling parameters and adjustments for tissue shrinkage could become amplified when calculating estimates of total population size and tissue volume (Keller et al., 2018). How the data derived from differing methods can be adjusted for comparison is not immediately clear. This variability combined with the tendency of most studies to examine only a select number of cell types complicates attempts to compare cell population sizes across studies.

To circumvent these issues, we sought to obtain estimates of a comprehensive set of cell types using consistent methodology. All data was generated using tissue from a single cohort of male and female mice of the C57BL/6 strain, one of the most commonly used rodent species in biosciences research (Bryant, 2011). Therefore, the main advantage of this dataset is the validity of internal comparisons between the various cell types of the DG in a common research model species. For example, when drawing comparisons based on data reported in separate studies, the neuron to astrocyte ratio could range from approximately 4.6:1 (Erö et al., 2018; Rajkowska et al., 2016) to 113:1 (Kurt et al., 2004; Olabarria et al., 2011). By comparison, using our estimates, we report a ratio of roughly 12 neurons:1 astrocyte, similar to the approximately 9:1 ratio reported by another group which estimated both neuron and astrocyte population size within a single study (Erö et al., 2018). This test case highlights the utility of counts obtained within a single study for making accurate comparisons of relative population sizes.

Important limitations to this dataset should be noted. Counts were performed exclusively in the dorsal (rostral/septal) DG with no separate delineation of the layers (i.e. molecular, granular, hilar) or inclusion of ventral DG populations. We chose to focus on whole dorsal DG because it represents a functional unit with known roles in mediating memory functions related to pattern separation and temporal encoding (Yassa and Stark, 2011). While the degree to which the DG dorsal-ventral axis constitutes discrete brain regions versus overlapping functional gradients is a matter of debate (Strange et al., 2014), distinct gene expression, connectivity, and behavioral correlates at the dorsal and ventral poles (Fanselow and Dong, 2010) provide justification for separate analysis. Given reports of disparate cell densities along the DG longitudinal axis (Jinno and Kosaka, 2010), future comprehensive studies should quantify the major cell populations for ventral DG, as well as for other neurogenic regions such as the subventricular zone and hypothalamus. Additionally, several of the cell populations quantified here could be meaningfully divided into additional subtypes (e.g. mature NeuN+ neurons into multiple excitatory and inhibitory subclasses and OLIG2+ cells into OPCs, immature oligodendrocytes, and mature oligodendrocytes) in future investigations.

Overall, we have provided stereological density estimates for the major cell lineages of the DG, which facilitates direct comparisons of their relative population sizes. We expect these data will be useful for refining hypotheses about how the activities of specific cell types relate to DG-mediated cognition. Similar quantification of other hippocampal subregions (e.g. CA regions) and extra-hippocampal regions (e.g. entorhinal cortex) would further enhance understanding of relative population numbers in the adult hippocampal circuit. These further characterizations of the hippocampus should be addressed in future work, as there are few studies that encompass the variety of cell types shown here.

### Conflict of Interest

*The authors declare that the research was conducted in the absence of any commercial or financial relationships that could be construed as a potential conflict of interest.*

### Author Contributions

PS and BMS processed and stained the tissue. EDK performed the stereological counts. JDR and EDK performed statistical analysis. JDR and EDK wrote the manuscript.

### Funding

This work was funded by R00NS089938 to EDK.

### Acknowledgements

The authors would like to thank Dr. Kathryn Lenz for use of equipment.

### References

Aimone, J.B., Wiles, J., and Gage, F.H. (2009). Computational Influence of Adult Neurogenesis on Memory Encoding. *Neuron* *61*, 187–202.

von Bohlen und Halbach, O. (2011). Immunohistological markers for proliferative events, gliogenesis, and neurogenesis within the adult hippocampus. *Cell And Tissue Research* *345*, 1–19.

Bonaguidi, M.A., Wheeler, M.A., Shapiro, J.S., Stadel, R.P., Sun, G.J., Ming, G., and Song, H. (2011). In Vivo Clonal Analysis Reveals Self-Renewing and Multipotent Adult Neural Stem Cell Characteristics. *Cell* *145*, 1142–1155.

Bryant, C.D. (2011). The blessings and curses of C57BL/6 substrains in mouse genetic studies. *Ann N Y Acad Sci* *1245*, 31–33.

Buscemi, L., Price, M., Bezzi, P., and Hirt, L. (2019). Spatio-temporal overview of neuroinflammation in an experimental mouse stroke model. *Sci Rep* *9*, 507.

Erö, C., Gewaltig, M.-O., Keller, D., and Markram, H. (2018). A Cell Atlas for the Mouse Brain. *Front. Neuroinform.* *12*.

Fanselow, M.S., and Dong, H.-W. (2010). Are the Dorsal and Ventral Hippocampus Functionally Distinct Structures? *Neuron* *65*, 7–19.

Gonçalves, J.T., Schafer, S.T., and Gage, F.H. (2016). Adult Neurogenesis in the Hippocampus: From Stem Cells to Behavior. *Cell* *167*, 897–914.

Gundersen, H.J.G., Jensen, E.B.V., Kiêu, K., and Nielsen, J. (1999). The efficiency of systematic sampling in stereology — reconsidered. *Journal of Microscopy* *193*, 199–211.

Jinno, S., and Kosaka, T. (2010). Stereological estimation of numerical densities of glutamatergic principal neurons in the mouse hippocampus. *Hippocampus* *20*, 829–840.

Keller, D., Erö, C., and Markram, H. (2018). Cell Densities in the Mouse Brain: A Systematic Review. *Frontiers in Neuroanatomy* *12*, 83.

Kirsch, G.W., Shen, J., Tian, M., Schroeder, B., Wang, J., Man, G., Wu, S., and Ge, S. (2017). Active Dentate Granule Cells Encode Experience to Promote the Addition of Adult-Born Hippocampal Neurons. *J. Neurosci.* *37*, 4661.

Knierim, J.J., and Neunuebel, J.P. (2016). Tracking the flow of hippocampal computation: Pattern separation, pattern completion, and attractor dynamics. *Neurobiology of Learning and Memory* *129*, 38–49.

Kuhn, H.G., Eisch, A.J., Spalding, K., and Peterson, D.A. (2016). Detection and Phenotypic Characterization of Adult Neurogenesis. *Cold Spring Harb Perspect Biol* *8*, a025981.

Kurt, M., Kafa, M., Dierssen, M., and Davies, D. (2004). Deficits of neuronal density in CA1 and synaptic density in the dentate gyrus, CA3 and CA1, in a mouse model of Down syndrome. *Brain Research* *1022*, 101–109.

Mandyam, C.D., Harburg, G.C., and Eisch, A.J. (2007). Determination of key aspects of precursor cell proliferation, cell cycle length and kinetics in the adult mouse subgranular zone. *Neuroscience* *146*, 108–122.

Michalovicz, L.T., Kelly, K.A., Vashishtha, S., Ben-Hamo, R., Efroni, S., Miller, J.V., Locker, A.R., Sullivan, K., Broderick, G., Miller, D.B., et al. (2019). Astrocyte-specific transcriptome analysis using the ALDH1L1 bacTRAP mouse reveals novel biomarkers of astrogliosis in response to neurotoxicity. *Journal of Neurochemistry* *150*, 420–440.

Miller, S.M., and Sahay, A. (2019). Functions of adult-born neurons in hippocampal memory interference and indexing. *Nature Neuroscience* *22*, 1565–1575.

Moreno-Jiménez, E.P., Flor-García, M., Terreros-Roncal, J., Rábano, A., Cafini, F., Pallas-Bazarría, N., Ávila, J., and Llorens-Martín, M. (2019). Adult hippocampal neurogenesis is abundant in neurologically healthy subjects and drops sharply in patients with Alzheimer's disease. *Nature Medicine* *25*, 554–560.

Olabarria, M., Noristani, H.N., Verkhratsky, A., and Rodríguez, J.J. (2011). Age-dependent decrease in glutamine synthetase expression in the hippocampal astroglia of the triple transgenic Alzheimer's disease mouse model: mechanism for deficient glutamatergic transmission? *Molecular Neurodegeneration* *6*, 55.

Rajkowska, G., Clarke, G., Mahajan, G., Licht, C.M.M., van de Werd, H.J.J.M., Yuan, P., Stockmeier, C.A., Manji, H.K., and Uylings, H.B.M. (2016). Differential effect of lithium on cell number in the hippocampus and prefrontal cortex in adult mice: a stereological study. *Bipolar Disord* *18*, 41–51.

Semerci, F., and Maletic-Savatic, M. (2016). Transgenic mouse models for studying adult neurogenesis. *Front Biol (Beijing)* *11*, 151–167.

Slomianka, L., and West, M.J. (2005). Estimators of the precision of stereological estimates: An example based on the CA1 pyramidal cell layer of rats. *Neuroscience* *136*, 757–767.

Smith, B.M., Yao, X., Chen, K.S., and Kirby, E.D. (2018). A Larger Social Network Enhances Novel Object Location Memory and Reduces Hippocampal Microgliosis in Aged Mice. *Frontiers in Aging Neuroscience* *10*, 142.

Sorrells, S.F., Paredes, M.F., Cebrian-Silla, A., Sandoval, K., Qi, D., Kelley, K.W., James, D., Mayer, S., Chang, J., Auguste, K.I., et al. (2018). Human hippocampal neurogenesis drops sharply in children to undetectable levels in adults. *Nature* *555*, 377–381.

Strange, B.A., Witter, M.P., Lein, E.S., and Moser, E.I. (2014). Functional organization of the hippocampal longitudinal axis. *Nature Reviews Neuroscience* *15*, 655–669.

Suh, H., Consiglio, A., Ray, J., Sawai, T., D'Amour, K.A., and Gage, F.H. (2007). In vivo fate analysis reveals the multipotent and self-renewal capacities of Sox2+ neural stem cells in the adult hippocampus. *Cell Stem Cell* *1*, 515–528.

Sultan, S., Li, L., Moss, J., Petrelli, F., Cassé, F., Gebara, E., Lopatar, J., Pfrieger, F.W., Bezzi, P., Bischofberger, J., et al. (2015). Synaptic Integration of Adult-Born Hippocampal Neurons Is Locally Controlled by Astrocytes. *Neuron* *88*, 957–972.

Tang, C., Wang, M., Wang, P., Wang, L., Wu, Q., and Guo, W. (2019). Neural Stem Cells Behave as a Functional Niche for the Maturation of Newborn Neurons through the Secretion of PTN. *Neuron* *101*, 32-44.e6.

Valério-Gomes, B., Guimarães, D.M., Szczupak, D., and Lent, R. (2018). The Absolute Number of Oligodendrocytes in the Adult Mouse Brain. *Front. Neuroanat.* *12*.

Wang, X.-X., Li, J.-T., Xie, X.-M., Gu, Y., Si, T.-M., Schmidt, M.V., and Wang, X.-D. (2017). Nectin-3 modulates the structural plasticity of dentate granule cells and long-term memory. *Transl Psychiatry* *7*, e1228.

Yassa, M.A., and Stark, C.E.L. (2011). Pattern separation in the hippocampus. *Trends in Neurosciences* *34*, 515–525.

## Figure Legends

**TABLE 1 | Antibodies used for immunohistochemical identification of cell phenotype.** All antibodies were validated in previous work or compared to an appropriate control to ensure specificity of immunolabeling.

**TABLE 2 | Total counts, distribution, error estimators, measured tissue thickness, and number of sections and sites sampled for all cell types surveyed in the current study.** For each cell type, the total cells counted and percentage of cells in the middle 5 consecutive 1  $\mu\text{m}$  z-sections and top 5 consecutive 1  $\mu\text{m}$  z-sections immediately below the guard zone are listed (mean  $\pm$  SEM). Error estimators are listed as Gunderson coefficients (with smoothness  $m = 0$  or  $m = 1$ ). For each round of immunostaining, the measured thickness (mean  $\pm$  SEM) as well as number of sampled slices and sites (mean  $\pm$  SEM) are provided. Thickness was manually measured in 3 locations per slice to adjust for shrinkage relative to the 40  $\mu\text{m}$  starting thickness.

**FIGURE 1 | Representative immunolabeling of neuronal, astroglial, oligodendroglial, microglial, endothelial, and proliferative cell markers in the dorsal dentate gyrus (DG). (A-B)** The ROI used for cell counts encompassed all layers of the DG and spanned the dorsal (rostral/septal) pole of the dorsal-ventral axis. **(C-E)** Representative SOX2 and GFAP immunolabeling. Mature astrocytes had SOX2+ nuclei, GFAP+ cytoplasm, and stellate morphology (**E, top, asterisk**). Radial glia-like neural precursors had SOX2+ nuclei in the SGZ, GFAP+ cytoplasm, and a radial process spanning the GCL (**E, bottom, arrows**). Neural intermediate progenitors had SOX2+ nuclei in the SGZ lacking GFAP+ cytoplasm (**E, bottom, chevrons**). **(F-H)** MCM2 immunolabeling and **(I-K)** BrdU immunolabeling 2 hours post injection to reveal actively cycling cells. **(L-N)** Representative immunolabeling of DCX+ neuroblasts/immature neurons and **(O-Q)** NeuN+ mature neurons. **(R-T)** Olig2 immunolabeling to detect oligodendroglial lineage cells. **(U-W)** Representative Iba1 immunolabeling for microglia. **(X-Z)** CD31 immunolabeling to detect vascular endothelial cells. Scale bars represent 100  $\mu\text{m}$  (**A, C, F, I, L, O, R, U, X**), 20  $\mu\text{m}$  (**D, G, J, M, P, S, V, Y**), or 10  $\mu\text{m}$  (**E, H, K, N, Q, T, W, Z**).

**FIGURE 2 | Stereological estimates of all cell types surveyed in the current study.** Data is represented as cell density (**A**) and number of cells in a 40  $\mu\text{m}$  slice (**B**). **(C)** Cell density estimates of mutually exclusive cell type categories (for example, MCM2+ cells might overlap with multiple other cell types and is thus not included). Data is mean  $\pm$  SEM from male ( $n = 5$ ) and female ( $n=4$ ) adult mice. No significant sex difference for any cell type was detected via unpaired, two-tailed t-test ( $p>0.05$ ).

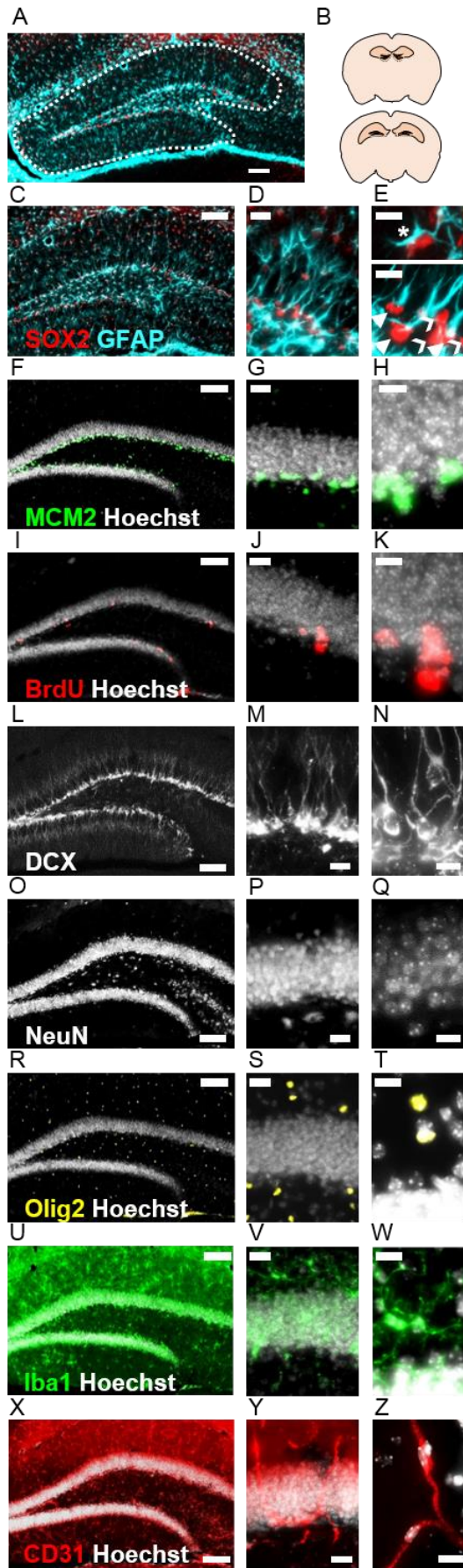
Primary antibodies							
Antibody	Host species	Cell type	Antigen retrieval	Vendor	Product #	Dilution	Ref/control
α Sox2	rat	NSC, NPC, astrocyte	None	eBioscience	14-9811	1:1000	Andersson-Rolf et al., 2017
α GFAP	rabbit	NSC, astrocyte	None	Dako	Z-0334	1:1000	Michalovicz et al., 2019
α MCM2	rabbit	Proliferating cells	None	Cell Signaling	4007	1:500	Wang et al., 2017
α BrdU	mouse	Proliferating cells	2N HCl, 37°C	BD Biosciences	BDB 347580	1:500	No BrdU injection
α DCX	rabbit	Immature neurons	None	Cell Signaling	4604	1:500	Tang et al., 2019
α NeuN	mouse	Neurons	None	EMD Millipore	MAB377	1:500	Buscemi et al., 2018
α Olig2	mouse	Oligodendrocyte lineage	None	EMD Millipore	MABN50	1:1000	Valério-Gomes et al., 2018
α Iba1	goat	Microglia	None	Abcam	Ab5076	1:2000	Smith et al., 2018
α CD31	rat	Endothelia	None	BD Pharmingen	550274	1:100	Buscemi et al., 2018

Secondary antibodies							
647 α rabbit	donkey	GFAP, MCM2, DCX	N/A	Invitrogen	A31573	1:500	No primary
594 α rat	donkey	Sox2, CD31	N/A	Invitrogen	A21209	1:500	No primary
488 α mouse	donkey	BrdU, NeuN	N/A	Invitrogen	A21202	1:500	No primary
488 α goat	donkey	Iba1	N/A	Invitrogen	A11055	1:500	No primary
555 α mouse	donkey	Olig2	N/A	Invitrogen	A31570	1:500	No primary

Cell type marker	Distribution						
	Total Cells Counted (mean $\pm$ SEM)	(% of all counted cells, mean $\pm$ SEM)		Gundersen- Jensen CE $m = 0$		Gundersen- Jensen CE $m = 1$	
		Top 5 $\mu$ m	Middle 5 $\mu$ m				
GFAP+SOX2+stel	308.1 $\pm$ 7.5	32.32 $\pm$ 0.95	37.55 $\pm$ 0.73	0.144		0.064	
GFAP+SOX2+rad	46.4 $\pm$ 4.1	34.44 $\pm$ 1.75	33.48 $\pm$ 2.37	0.203		0.154	
GFAP-SOX2+	148.3 $\pm$ 8.2	30.07 $\pm$ 2.17	36.06 $\pm$ 1.83	0.164		0.088	
MCM2	140.1 $\pm$ 10.5	38.47 $\pm$ 3.69	33.63 $\pm$ 2.52	0.188		0.094	
BrdU	22.7 $\pm$ 2.7	37.25 $\pm$ 5.32	20.58 $\pm$ 5.46	0.287		0.243	
DCX	217.6 $\pm$ 14.7	33.27 $\pm$ 2.67	34.94 $\pm$ 1.88	0.161		0.078	
NeuN	325.8 $\pm$ 21.6	36.60 $\pm$ 1.15	37.80 $\pm$ 0.88	0.183		0.068	
Olig2	111.6 $\pm$ 10.6	35.99 $\pm$ 4.06	33.05 $\pm$ 3.02	0.169		0.101	
Iba1	74.3 $\pm$ 6.6	35.49 $\pm$ 0.76	34.75 $\pm$ 1.76	0.164		0.120	
CD31	175.1 $\pm$ 7.7	30.21 $\pm$ 1.15	39.07 $\pm$ 1.97	0.161		0.083	
Immunostaining Round	Measured Tissue Thickness (mean $\pm$ SEM)			Sections surveyed	Number of sites surveyed (mean $\pm$ SEM)		
	Males	Females					
	25.3 $\pm$ 0.09	26.6 $\pm$ 1.33		3	56.8 $\pm$ 1.3		
GFAP, SOX2, BrdU	25.9 $\pm$ 0.80	24.8 $\pm$ 0.75		3	60.6 $\pm$ 1.3 (DCX, CD31) 62.9 $\pm$ 3.3 (NeuN)		
DCX, NeuN, CD31	26.3 $\pm$ 0.69	25.5 $\pm$ 0.86		3	59.7 $\pm$ 1.5		

## Stereological Characterization of Mouse DG



## Stereological Characterization of Mouse DG

